

Spectral Energy Distributions for TeV Blazars

C. Lin^{1,2} ^{***} and J. H. Fan^{1,2} [†]

¹ Center for Astrophysics, Guangzhou University, Guangzhou 510006, China;

² Astronomy Science and Technology Research Laboratory of Department of Education of Guangdong Province, Guangzhou 510006, China

Received [year] [month] [day]; accepted [year] [month] [day]

Abstract In this work, we collected a sample of 69 TeV blazars from TeVCat, obtained their multi-wavelength observations, and fitted their spectral energy distributions by using the second degree polynomial function. The structure parameters of the synchrotron bumps for 68 blazars and those of the inverse-Compton bumps for 56 blazars are obtained. Then, we adopted statistical analysis to the parameters (curvature, peak frequency, peak luminosity, bolometric luminosity, and X/γ-ray spectral indexes). From our analysis and discussions, we can get following conclusions: 1. There is a clear positive correlation between the synchrotron peak frequency, $\log \nu_p^s$, and the inverse-Compton peak frequency $\log \nu_p^{IC}$, and that between the synchrotron peak luminosity, $\log \nu_p^s L_{\nu_p^s}$, and the inverse-Compton peak luminosity, $\log \nu_p^{IC} L_{\nu_p^{IC}}$. 2. The correlation between the peak frequency and the curvature of synchrotron bump is clearly different from that of the inverse-Compton bump, which further indicates that there are different emission mechanisms between them. 3. There is a correlation between $\log \nu_p^{IC}$ and γ-ray spectral index, α_γ , for the TeV blazars: $\log \nu_p^{IC} = -(4.59 \pm 0.30)\alpha_\gamma + (32.67 \pm 0.59)$, which is consistent with previous work of Abdo et al.(2010). 4. An "L-shape" relation is found between $\log \nu_p^s$ and α_X for both TeV blazars and Fermi blazars. A significant correlation between $\log \nu_p^s$ and X-ray photon index (α_X) is found for the TeV blazars with high synchrotron peak frequency: $\log \nu_p^s = -(3.20 \pm 0.34)\alpha_X + (24.33 \pm 0.79)$, while the correlation is positive for low synchrotron peaked TeV sources. 5. In the $\alpha_X - \alpha_\gamma$ diagram, there is also an "L-shape", the anti-correlation is consistent with the available results in the literature, we also find a positive correlation between them. 6. Inverse-Compton dominant sources have luminous bolometric luminosities.

Key words: galaxies: active-BL Lacertae objects: general-quasars: general-galaxies: jets;

1 INTRODUCTION

Blazars are a subclass of the radio-loud active galactic nuclei (AGNs) with extreme observational properties, such as high and variable polarization, rapid and large variability in the non-thermal continuum, strong γ-ray emissions, and superluminal motions, etc (Urry & Padovani 1995; Fan 2005). In a standard AGN model, there is a supermassive black hole surrounded by an accretion disk at the center, and there is a high speed jet perpendicular to the accretion disk. Blazars are believed to be a subclass of AGNs

^{***} linchao@e.gzhu.edu.cn

[†] Corresponding author: fjh@gzhu.edu.cn

whose jet axis is very close to the line of the observer's sight. Blazars are divided into flat spectrum radio quasars (FSRQs) and BL Lacertae objects (BL Lacs). BL Lacs and FSRQs show similar continuum emission properties with BL Lacs showing weak (or even no) emission line features but FSRQs displaying strong emission lines (Aller et al. 1992; Urry & Padovani 1995; Fan et al. 2009; Hovatta et al. 2009; Lin et al. 2017).

Recently, the emissions of TeV band, which are also called as very-high-energy band (VHE; $E > 100$ GeV), are detected from an increasing number of extragalactic sources (Acero et al. 2015). TeVCat¹ is an online catalog for VHE γ -Ray Astronomy, collecting the sources that have been detected by the ground-base telescopes (Wakely & Horan 2008). TeV emissions are important to constrain the emission mechanism of AGNs and studied by some researchers (eg., Weekes 1997; Giannios et al. 2009; Piner et al. 2010; Holder 2012; Zhang et al. 2012; Xiong et al. 2013; Aartsen et al. 2015; Lin & Fan 2016; Sahu et al. 2016).

The broad-band SEDs of blazars show a double bump structure in the flux ($\log \nu f_\nu$) versus frequency ($\log \nu$) panel. The low energy bump commonly peaks at infrared to X-ray bands, while the high energy one peaks at MeV-GeV band (Fossati et al. 1998; Kang et al. 2014). It is generally accepted that the low energy bump is corresponding to a synchrotron emission which is produced by the relativistic electrons in the jet, while the high energy bump is corresponding to an inverse-Compton (IC) emission which is caused by the IC scattering. However, different authors have different ideas about the origins of the seed photons of IC process. Some researchers think that IC process is from synchrotron self-Compton (SSC) process with the seed photons being from synchrotron emissions in the jet (eg., Rees et al. 1967; Jones et al. 1974; Marscher & Gear 1985; Mastichiadis et al. 1997; Krawczynski et al. 2001; Sikora et al. 2001; Abdo et al. 2014; Hovatta et al. 2015; Yang et al. 2017a,b). Others believe that the seed photons are from exterior of the jet, such as accretion disk, broad line region, dust torus and so on, and that is called external Compton (EC) process (eg., Dermer et al. 1992; Dermer & Schlickeiser 1993; Sikora et al. 1994; Hartman et al. 2001; Sokolov & Marscher 2005; Albert et al. 2008). Another classification of blazars is the one based on their synchrotron peak frequency of the spectral energy distributions (SEDs) (Padovani & Giommi 1995; Nieppola et al. 2006; Abdo et al. 2010a; Ackermann et al. 2015; Lin & Fan 2016; Fan et al. 2016). In our previous work (Fan et al. 2016), we divided blazars into low synchrotron peaked (LSP, $\nu_{\text{peak}}^s < 10^{14}$ Hz), intermediate synchrotron peaked (ISP, 10^{14} Hz $< \nu_{\text{peak}}^s < 10^{15.3}$ Hz), and high synchrotron peaked (HSP, $\nu_{\text{peak}}^s > 10^{15.3}$ Hz) blazars by analyzing a sample of 1329 blazars.

In this work, we collect a sample of 69 TeV blazars from TeVCat, and try to keep track of all announced TeV sources, so that our sample is the largest for TeV blazars until April 2018. Because only one TeV blazars (1943 + 213) is not detected by Fermi telescope, and the dominant power of IC bump is at Fermi observational band, we assume that TeV blazars are, not strictly, a sub-sample of Fermi blazars only for statistical comparison in this work. We use a second degree polynomial function to fit their multiwavelength SEDs, obtain fitting parameters, calculate monochromatic luminosity and bolometric luminosity. This paper is arranged as follows: We will give a sample and fitting procedure in Section 2, results in Section 3, some discussions and conclusions in Sections 4 and 5.

2 SAMPLE AND FITTING PROCEDURE

From TeVCat, we found that there are 210 sources detected in TeV energy range until April 2018, and 75 (69 blazars) of them are the extragalactic TeV sources with low redshift ($z < 1.0$). Most of the TeV blazars are HSP BL Lacs, which are usually considered to be the candidates of the extragalactic TeV sources (Lin & Fan 2016, and reference therein). The connection between TeV source and peak frequency is still an interesting topic of blazars.

A useful tool for building SEDs in Space Science Data Center (SSDC) is SSDC SED Builder², which combines radio to γ -ray (even TeV) band data from several missions and experiments together

¹ <http://tevcat.uchicago.edu/>

² <http://tools.asdc.asi.it/SED/>

with catalogs and archival data (Aharonian et al. 2001; Giommi et al. 2002; Amenomori et al. 2003; Aharonian et al. 2003, 2009; Daniel et al. 2005; Schroedter et al. 2005; Acciari et al. 2008, 2011; Godambe et al. 2008; Chandra et al. 2010, 2012; H.E.S.S. Collaboration 2010, 2013; Aliu et al. 2011, 2015; Bartoli et al. 2011, 2012; Archambault et al. 2013, 2014; Arlen et al. 2013; Abramowski et al. 2013, 2015; Biteau & Williams 2015; Sharma et al. 2015). In this work, we collect 69 blazars (62 BL Lacs and 7 FSRQs) from TeVCat, and obtain their SEDs by using SSDC SED Builder. We use the default search radius values in SSDC SED Builder to search the observational data from the corresponding databases, and reject the data whose flux error is larger than flux and the upper limit data. We find that some observational data ($\nu > 10^{16}$ Hz) from the NASA/IPAC Extragalactic Database (NED)³ is significantly different from other databases. Because the data from NED is collected from different archives which use different methods to calculate the observational data, thus we neglected the data whose $\nu > 10^{16}$ Hz from NED in this work.

In order to unify the fitting procedure for each source, we did not consider the observational time of the data, unless the wide range of time causing the fitting result unreliable. For example, if several times of flare are detected in TeV band, we choose an time interval to keep the latest observation of flare. Observations indicate that the thermal radiation is exist and causes a bump at UV/optical bands of SEDs for some AGNs (eg., Shields 1978; Czerny & Elvis 1987; Ross et al. 1992; Mannheim et al. 1995; Pounds et al. 1995). We exclude the thermal radiation of the source by visual inspection, because the thermal radiation is significantly greater than the non-thermal radiation at UV/optical bands. Similarly, we determine the break point between two bumps by visual inspection, and then fit the two bumps respectively.

In this work, we found that the SEDs of some sources are asymmetrical in synchrotron bump, such as 0721+713, especially in low energy radio band ($\log \nu < 10^9$ Hz). Since the second degree polynomial function is symmetrical, it is better that those SEDs are fitting by a third degree polynomial function. The third degree polynomial function is an empirical fitting function in SEDs calculations, and used in many works (eg., Fossati et al. 1998; Kubo et al. 1998; Abdo et al. 2010b; Wu et al. 2011; Ackermann et al. 2015; Chang et al. 2017). The asymmetrical structures of SEDs are possibly produced by some physical process, such as the synchrotron self-absorption process.

But, there are also many works indicate that the structure of SEDs is symmetric for blazars (eg., Landau et al. 1986; Sambruna et al. 1996; Zhang et al. 2002; Massaro et al. 2004a, b, 2006; Nieppola et al. 2006; Wu et al. 2009; Meyer et al. 2011; Xue et al. 2016; Fan et al. 2016). Massaro (2004b) found that the log-parabolic spectral model is not only the simplest way to fit the SEDs of Mrk 421, but also relates to the physics of the statistical acceleration process under some simple hypotheses. In the work of Xue et al. (2016), they discussed the difference of luminosity between the second and third degree polynomial fitting for some sources with apparent asymmetrical synchrotron bump. They found that the logarithm of luminosity in third degree polynomial fitting is lower than that in second degree polynomial fitting, and the differences are within 1.

The three parameters of the second degree polynomial function can give the basic structure of the SEDs, namely, the spectral curvature, the peak frequency, and the peak flux. For analyzing the basic structure of the SEDs for blazars, we prefer to use the second degree polynomial, the reasons are: 1. the second degree polynomial is enough for determining the basic structure; 2. Most of the SEDs of TeV blazars are symmetrical in this work; 3. As discussed in Xue et al. (2016), the difference of luminosity between the second and third degree polynomial fitting is insignificant; 4. It is hard to give a meaningful definition of each parameter for the third degree polynomial.

Following our previous work (Fan et al. 2016), we can fit the synchrotron bump and IC bump of SEDs using the following function:

$$\log(\nu f_\nu) = c(\log \nu - \log \nu_p)^2 + \log \nu_p f_{\nu_p}, \quad (1)$$

where $|2c|$ is the spectral curvature, $\log \nu_p$ is the logarithm of peak frequency, and $\log \nu_p f_{\nu_p}$ is the logarithm of peak flux. In order to reduce the effect of fitting from asymmetrical SEDs, we set the lower

³ <http://ned.ipac.caltech.edu/>

limit of the frequency to $\nu = 10^9$ Hz in the second degree polynomial fitting. Comparing with other energetic bands, optical band has plenty observational data for some sources. Consequently, when the least square method is adopted to fit the SEDs, the second degree polynomial fitting will be dominant by the optical band. To rebalance the weights between different bands, we calculate the averaged fluxes and frequencies for each frequency bin by using the following formulas:

$$\log(\nu f_\nu) = \frac{\sum_{i=1}^n \frac{\log(\nu_i f_i)}{err_i^2}}{\sum_{i=1}^n \frac{1}{err_i^2}}, \quad (2)$$

$$\log \nu = \frac{\sum_{i=1}^n \frac{\log \nu_i}{err_i^2}}{\sum_{i=1}^n \frac{1}{err_i^2}}, \quad (3)$$

where $err^2 = err_+^2 + err_-^2$, err_+ and err_- are the positive and negative errors of $\log(\nu f_\nu)$, and we set the bin width to be $\Delta(\log \nu) = 0.1$. For the flux without error, we use the averaged value of neighboring errors to replace it.

Peak luminosity ($\nu_p L_p$) and bolometric luminosity (L_{bol}) in source rest frame are calculated using the following formulas:

$$\nu_p L_p = 4\pi d_L^2 \nu_p' f_{\nu_p}' \quad (4)$$

$$L_{bol} = 4\pi d_L^2 \ln(10) \int_{\log \nu_L}^{\log \nu_U} 10^{c(\log \nu - \log \nu_p')^2 + \log \nu_p' f_{\nu_p}'} d(\log \nu) \quad (5)$$

where $d_L = (1+z) \frac{c}{H_0} \int_1^{1+z} \frac{1}{\sqrt{\Omega_M x^3 + 1 - \Omega_M}} dx$ is luminosity distance, $\nu_p' = (1+z)\nu_p$, $f_{\nu_p}' = f_{\nu_p}(1+z)^{\alpha_p-1}$, $(1+z)^{\alpha_p-1}$ stands for K-correction, and $\alpha_p = -\partial \log f_\nu / \partial \log \nu = 1$ is a spectral index at the peak frequency. Average value is adopted in K-correction if the redshift of the source is not available. In this work, we set the lower and upper limits of integration to be $\nu_L = 10^9$ Hz and $\nu_U = 10^{27}$ Hz. We adopt $\Omega_\Lambda \simeq 0.7$, $\Omega_M \simeq 0.3$ and $\Omega_K \simeq 0.0$ from the Λ -CDM model (Capelo & Natarajan 2007), and $H_0 = 67 \text{ km s}^{-1} \text{ Mpc}^{-1}$.

3 RESULTS

We fit the SEDs for the whole 69 TeV blazars using the second degree polynomial function. Because the observations are scarce or do not cover enough range of frequency, we can not fit the SEDs reliable for some sources. Finally, the fitting results of synchrotron bump for 68 blazars and those of IC bump for 56 blazars are obtained. The SEDs fitting results for the 69 blazars are shown in Figures 1-2. In Figures 1-2, the thermal radiation data are included in the figure but they are excluded in the SED fitting. The curves in the figures stand for the fitting results. If some time intervals are selected for some sources in TeV band, then only the data in the chosen time interval are shown in the figures.

For statistical analysis, X-ray spectral index from Swift-XRT point source catalog (1SXPS, Evans et al. 2014) and γ -ray spectral index from the third Fermi Large Area Telescope source catalog (3FGL) are also collected. The sample and fitting results in observer frame are shown in Table 1. Particularly, the redshift effect of peak luminosity and bolometric luminosity are already corrected, see Equations (4) and (5). In Table 1, Col. (1) gives TeVCat name; Col. (2) other name, the sources with "*" are FSRQs, the rests are BL Lacs; Col. (3) redshift (z); Col. (4) the spectral curvature ($|2c^s|$) of synchrotron bump and its uncertainty; Col. (5) synchrotron peak frequency ($\log \nu_p^s$) in units of Hz and its uncertainty; Col. (6) synchrotron peak flux ($\log \nu_p^s f_{\nu_p^s}$) in units of erg/cm²/s and its uncertainty; Col. (7) the spectral curvature ($|2c^{IC}|$) of IC bump and its uncertainty; Col. (8) IC peak frequency ($\log \nu_p^{IC}$) in units of Hz and its uncertainty; Col. (9) IC peak flux ($\log \nu_p^{IC} f_{\nu_p^{IC}}$) in units of erg/cm²/s and its uncertainty; Col. (10) bolometric luminosity ($\log L_{bol}$) in units of erg/s; Col. (11) γ -ray photon index (α_γ) from 3FGL; Col. (12) X-ray photon index (α_X) from 1SXPS. The statistical values of the fitting results are show in Table 2. In Table 2 and the following statistical analysis, frequencies, fluxes and luminosities are corrected to the sources' rest-frame.

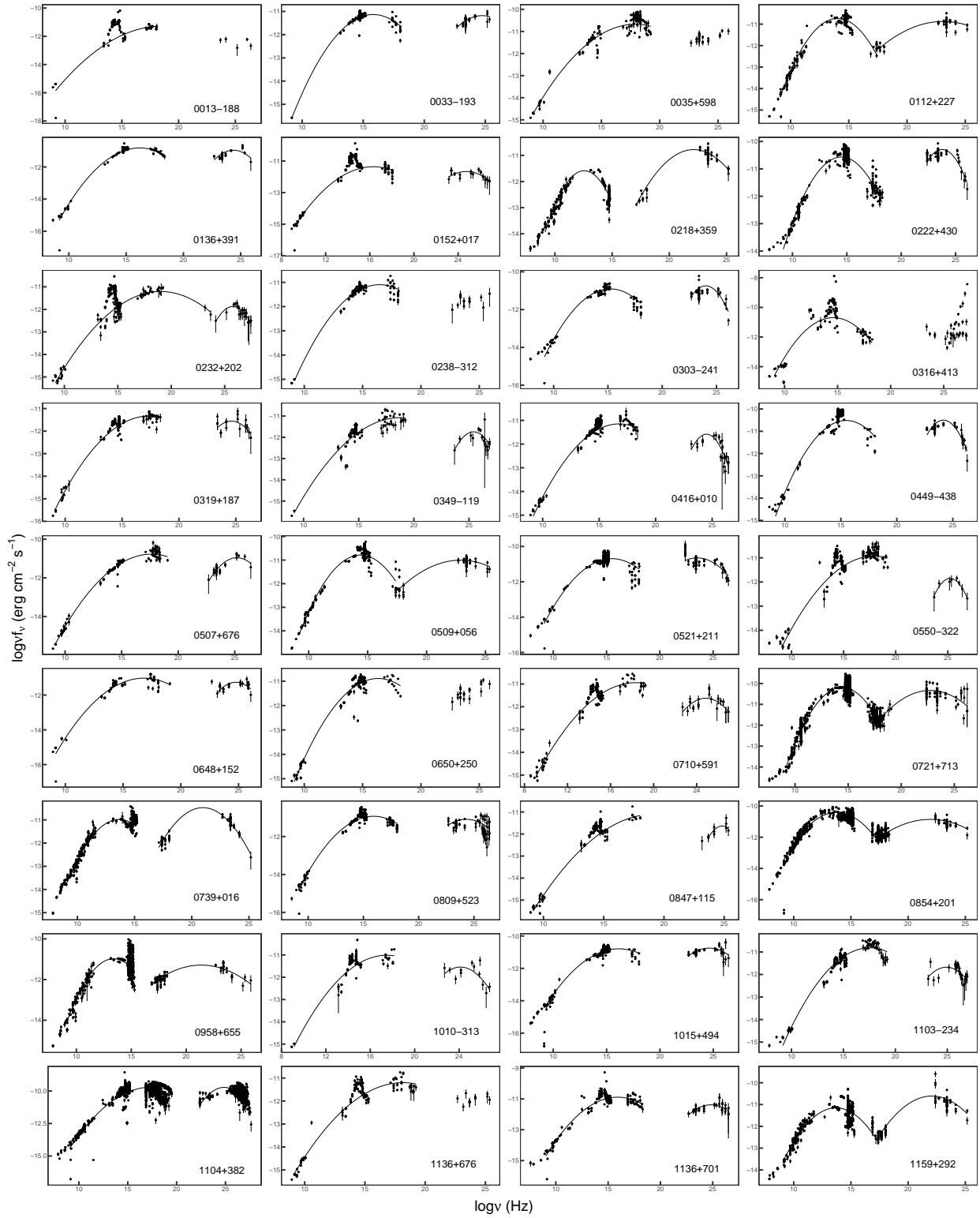


Fig. 1 Spectral Energy Distributions for TeV Blazars.

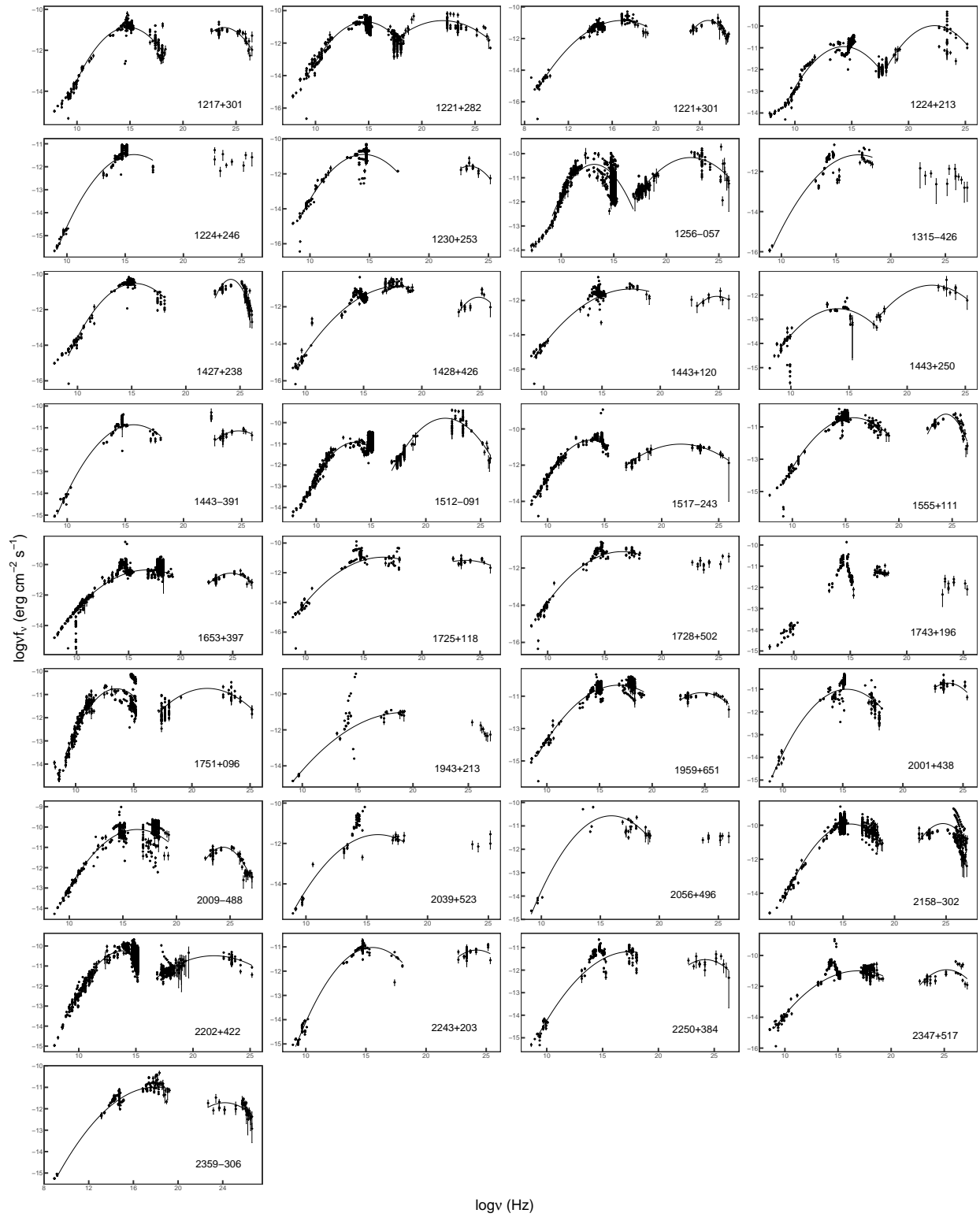


Fig. 2 Spectral Energy Distributions for TeV Blazars.

Table 1: The Fitting Results in observed frame for 69 TeV Blazars.

TeV Cat name	other name	z	$ 2c^s /\sigma$	$\log \nu_p^s/\sigma$	$\log \nu_p^s f_{\nu_p^s}/\sigma$	$ 2c^{IC} /\sigma$	$\log \nu_p^{IC}/\sigma$	$\log \nu_p^{IC} f_{\nu_p^{IC}}/\sigma$	$\log L_{bol}$	α_γ	α_X
(1)	(2)	(3)	(4)	(5)	(6)	(7)	(8)	(9)	(10)	(11)	(12)
J0013-188	SHBLJ001355.9-1854	0.094	0.10/0.01	18.56/0.58	-11.28/0.10					1.94	2.12
J0033-193	KUV00311-1938	0.61	0.20/0.01	15.82/0.05	-11.13/0.02	0.24/0.13	24.75/0.41	-11.18/0.06	47.41	1.71	2.47
J0035+598	1ES0033+595	0.086	0.11/0.01	17.91/0.40	-10.68/0.06					1.90	2.04
J0112+227	S20109+22	0.265	0.30/0.01	14.03/0.07	-10.73/0.05	0.08/0.01	23.11/0.32	-10.88/0.04	46.87	2.03	1.87
J0136+391	RGBJ0136+391		0.18/0.01	16.18/0.07	-10.81/0.02	0.43/0.21	24.37/0.20	-10.96/0.15		1.70	2.41
J0152+017	RGBJ0152+017	0.08	0.15/0.01	16.32/0.18	-11.36/0.04	0.27/0.10	24.75/0.19	-11.66/0.10	44.96	1.89	2.51
J0218+359	S30218+35*	0.944	0.41/0.03	12.56/0.05	-11.59/0.07	0.17/0.01	22.13/0.13	-10.78/0.07	48.14	2.28	1.75
J0222+430	3C66A	0.444	0.24/0.01	14.50/0.05	-10.57/0.05	0.46/0.11	23.77/0.15	-10.29/0.09	47.68	1.94	2.27
J0232+202	1ES0229+200	0.139	0.08/0.01	19.01/0.14	-11.21/0.03	0.52/0.08	25.77/0.08	-11.87/0.06	45.67	2.03	1.92
J0238-312	1RXSJ023832.6-3116	0.232	0.15/0.01	16.46/0.16	-11.10/0.04					1.84	2.67
J0303-241	PKS0301-243	0.26	0.20/0.01	15.22/0.09	-10.90/0.03	0.63/0.18	24.02/0.18	-10.74/0.15	46.67	1.92	2.49
J0316+413	IC310	0.019	0.25/0.03	14.59/0.17	-10.69/0.19					1.90	
J0319+187	RBS0413	0.19	0.12/0.01	17.35/0.19	-11.33/0.03	0.39/0.25	24.61/0.28	-11.55/0.17	45.88	1.57	2.20
J0349-119	1ES0347-121	0.188	0.10/0.01	18.77/0.44	-11.07/0.07	0.59/0.15	25.31/0.11	-11.79/0.11	46.08	1.73	2.01
J0416+010	1ES0414+009	0.287	0.13/0.01	16.77/0.16	-11.15/0.03	0.73/0.20	24.50/0.15	-11.58/0.16	46.42	1.75	2.38
J0449-438	PKS0447-439	0.205	0.22/0.01	15.46/0.13	-10.52/0.05	0.62/0.14	24.16/0.13	-10.50/0.13	46.73	1.85	2.70
J0507+676	1ES0502+675	0.34	0.13/0.01	17.64/0.16	-10.77/0.03	0.39/0.11	25.19/0.23	-10.96/0.10	47.06	1.52	2.30
J0509+056	TXS0506+056		0.25/0.01	14.40/0.10	-10.79/0.04	0.09/0.02	22.89/0.48	-11.00/0.09		2.04	2.32
J0521+211	VERJ0521+211	0.108	0.18/0.01	15.50/0.11	-10.69/0.03	0.24/0.11	23.50/0.52	-10.65/0.11	46.03	1.92	2.35
J0550-322	PKS0548-322	0.069	0.10/0.02	17.92/0.60	-10.93/0.07	0.61/0.08	25.23/0.06	-11.85/0.06	45.23	1.61	1.86
J0648+152	RXJ0648.7+1516	0.179	0.15/0.01	16.80/0.21	-11.03/0.06	0.46/0.23	24.76/0.17	-11.26/0.15	46.08	1.83	2.36
J0650+250	1ES0647+250	0.203	0.16/0.01	16.33/0.18	-10.89/0.05					1.72	2.33
J0710+591	RGBJ0710+591	0.125	0.10/0.01	18.34/0.55	-10.94/0.07	0.26/0.08	24.84/0.16	-11.63/0.10	45.81	1.66	1.79
J0721+713	S50716+714	0.127	0.27/0.01	14.43/0.04	-10.19/0.04	0.12/0.02	22.72/0.21	-10.33/0.11	46.63	2.04	2.18
J0739+016	PKS0736+01*	0.189	0.26/0.01	13.66/0.09	-10.98/0.03	0.23/0.02	20.98/0.06	-10.47/0.12	46.58	2.48	1.70
J0809+523	1ES0806+524	0.138	0.17/0.01	15.91/0.12	-10.93/0.03	0.22/0.12	24.31/0.28	-11.09/0.11	45.96	1.88	2.49
J0847+115	RBS0723	0.199	0.10/0.01	18.54/0.23	-11.22/0.07	0.29/0.28	25.27/1.07	-11.70/0.12	46.03	1.74	1.93
J0854+201	OJ287	0.306	0.28/0.01	13.76/0.07	-10.41/0.05	0.12/0.02	21.94/0.22	-10.86/0.09	47.19	2.18	1.72
J0958+655	S40954+65	0.367	0.34/0.02	13.38/0.08	-10.98/0.05	0.09/0.01	21.37/0.12	-11.29/0.08	46.88	2.38	1.69
J1010-313	1RXSJ101015.9-3119	0.143	0.12/0.02	17.47/0.49	-11.01/0.10	0.29/0.15	24.12/0.42	-11.54/0.17	45.86	1.58	2.33
J1015+494	1ES1011+496	0.212	0.15/0.01	16.14/0.17	-10.79/0.04	0.26/0.10	24.61/0.16	-10.75/0.09	46.62	1.83	2.54
J1103-234	1ES1101-232	0.186	0.12/0.01	17.53/0.26	-10.82/0.05	0.28/0.13	24.92/0.21	-11.68/0.14	46.28	1.64	2.05
J1104+382	mrk421	0.031	0.14/0.01	17.38/0.31	-9.71/0.07	0.44/0.06	24.87/0.09	-9.72/0.10	45.81	1.77	2.29
J1136+676	RXJ1136.5+6737	0.136	0.10/0.01	18.15/0.61	-11.20/0.08					1.72	1.92
J1136+701	Mrk180	0.045	0.16/0.01	15.91/0.21	-10.89/0.08	0.29/0.09	24.82/0.15	-11.39/0.09	44.84	1.82	2.38
J1159+292	TON0599*	0.725	0.23/0.02	13.69/0.11	-11.15/0.07	0.17/0.02	22.08/0.15	-10.61/0.07	48.02	2.21	1.68
J1217+301	1ES1215+303	0.13	0.22/0.01	14.81/0.05	-10.88/0.04	0.32/0.10	23.87/0.30	-10.89/0.10	45.95	1.97	2.65
J1221+282	WComae	0.103	0.23/0.01	14.66/0.07	-10.69/0.04	0.12/0.03	21.96/0.22	-10.62/0.16	46.06	2.10	2.41
J1221+301	1ES1218+304	0.182	0.15/0.01	16.87/0.15	-10.86/0.04	0.62/0.09	24.75/0.07	-10.85/0.09	46.32	1.66	2.14
J1224+213	4C+21.35*	0.435	0.21/0.01	14.30/0.11	-10.94/0.05	0.22/0.04	22.29/0.21	-9.98/0.14	47.93	2.29	1.57

Table 1: Continue.

TeVcat name	other name	z	$ 2c^s /\sigma$	$\log \nu_p^s/\sigma$	$\log \nu_p^s f_{\nu_p^s}/\sigma$	$ 2c^{IC} /\sigma$	$\log \nu_p^{IC}/\sigma$	$\log \nu_p^{IC} f_{\nu_p^{IC}}/\sigma$	$\log L_{bol}$	α_γ	α_X
(1)	(2)	(3)	(4)	(5)	(6)	(7)	(8)	(9)	(10)	(11)	(12)
J1224+246	MS1221.8+2452	0.219	0.19/0.02	15.76/0.34	-11.47/0.08					1.89	
J1230+253	S31227+25	0.135	0.25/0.02	14.52/0.14	-10.89/0.05	0.48/0.27	23.41/0.38	-11.56/0.11	45.76	2.24	
J1256-057	3C279*	0.536	0.27/0.02	13.14/0.10	-10.44/0.06	0.12/0.02	22.31/0.17	-10.16/0.09	48.21	2.34	1.60
J1315-426	1ES1312-423	0.105	0.15/0.03	17.04/0.57	-11.17/0.14					2.08	2.11
J1427+238	PKS1424+240	0.16	0.22/0.01	15.30/0.10	-10.53/0.04	0.98/0.17	24.15/0.09	-10.30/0.14	46.51	1.82	2.64
J1428+426	H1426+428	0.129	0.11/0.01	17.99/0.40	-10.89/0.06	0.56/0.40	24.87/0.35	-11.48/0.22	45.86	1.57	2.06
J1443+120	1ES1440+122	0.163	0.11/0.01	17.50/0.26	-11.33/0.05	0.41/0.16	24.85/0.20	-11.76/0.09	45.68	1.80	2.06
J1443+250	PKS1441+25*	0.939	0.18/0.04	13.49/0.32	-12.50/0.10	0.13/0.02	22.13/0.21	-11.58/0.08	47.38	2.13	
J1443-391	PKS1440-389	0.065	0.19/0.01	15.71/0.14	-10.86/0.04	0.22/0.06	24.73/0.17	-11.14/0.04	45.25	1.81	2.64
J1512-091	PKS1510-089*	0.36	0.26/0.02	13.56/0.11	-10.92/0.04	0.21/0.02	21.77/0.08	-9.79/0.09	47.90	2.36	1.28
J1517-243	APLibrae	0.048	0.28/0.01	13.81/0.09	-10.62/0.03	0.10/0.01	21.67/0.07	-10.84/0.04	45.25	2.11	1.61
J1555+111	PG1553+113	0.36	0.19/0.01	15.70/0.06	-10.43/0.03	0.84/0.11	24.41/0.06	-10.21/0.11	47.50	1.68	2.42
J1653+397	mrk501	0.034	0.11/0.01	16.83/0.20	-10.35/0.05	0.31/0.06	24.82/0.09	-10.57/0.08	45.23	1.72	2.11
J1725+118	H1722+119	0.018	0.14/0.02	16.70/0.44	-10.95/0.08	0.15/0.14	23.75/0.74	-11.16/0.10	44.08	1.89	2.74
J1728+502	1ES1727+502	0.055	0.13/0.01	16.53/0.28	-11.12/0.05					1.96	2.28
J1743+196	1ES1741+196	0.084								1.78	2.17
J1751+096	OT081	0.322	0.30/0.04	13.52/0.19	-10.75/0.07	0.12/0.02	21.31/0.11	-10.74/0.08	47.13	2.25	1.79
J1943+213	HESSJ1943+213		0.08/0.01	19.25/0.52	-11.03/0.06						
J1959+651	1ES1959+650	0.047	0.15/0.01	16.82/0.17	-10.32/0.05	0.22/0.05	24.73/0.15	-10.78/0.08	45.48	1.88	2.32
J2001+438	MAGICJ2001+435		0.20/0.01	15.34/0.13	-11.00/0.06	0.33/0.20	23.76/0.30	-10.73/0.10		1.97	2.54
J2009-488	PKS2005-489	0.071	0.14/0.01	16.33/0.17	-10.12/0.06	0.45/0.05	24.36/0.09	-10.99/0.07	45.99	1.77	2.62
J2039+523	1ES2037+521	0.053	0.16/0.02	15.92/0.37	-11.56/0.13					1.89	2.62
J2056+496	RGBJ2056+496		0.18/0.02	15.94/0.22	-10.57/0.13					1.78	2.42
J2158-302	PKS2155-304	0.116	0.21/0.01	15.73/0.07	-9.93/0.04	0.39/0.10	24.69/0.15	-9.90/0.16	46.79	1.83	2.64
J2202+422	BLLac	0.069	0.27/0.02	13.90/0.10	-10.24/0.03	0.09/0.01	21.84/0.23	-10.49/0.07	45.97	2.25	1.79
J2243+203	RGBJ2243+203		0.20/0.01	15.54/0.10	-11.03/0.04	0.24/0.23	24.21/0.39	-11.13/0.14		1.79	2.76
J2250+384	B32247+381	0.119	0.11/0.01	17.47/0.56	-11.18/0.09	0.21/0.15	24.20/0.39	-11.53/0.14	45.56	1.91	2.43
J2347+517	1ES2344+514	0.044	0.12/0.01	16.90/0.24	-11.00/0.05	0.31/0.13	25.22/0.22	-10.93/0.19	44.91	1.78	2.09
J2359-306	H2356-309	0.165	0.11/0.01	18.02/0.38	-10.99/0.04	0.19/0.11	24.19/0.41	-11.72/0.12	46.03	2.02	2.07

Table 2 Statistical Values for the Fitting Results.

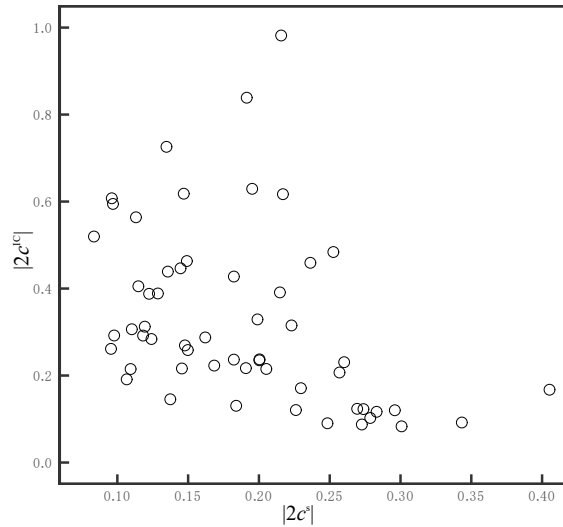
Parameter	min	max	mean	std
$ 2c^s $	0.08	0.41	0.18	0.07
$\log \nu_p^s$	12.85	19.31	16.07	1.62
$\log \nu_p^s f_{\nu_p^s}$	-12.21	-9.70	-10.81	0.39
$ 2c^{IC} $	0.08	0.98	0.33	0.20
$\log \nu_p^{IC}$	21.05	25.83	23.90	1.24
$\log \nu_p^{IC} f_{\nu_p^{IC}}$	-11.82	-9.66	-10.89	0.57
$\log L_{bol}$	44.08	48.21	46.31	0.93

3.1 Curvature and Peak Frequency

From our fitting results, we plot the curvature of IC bump against that of the synchrotron bump in Figure 3. Based on a T-test, we find that the curvature of IC bump is, on average, higher than that of synchrotron bump with a chance probability $p < 10^{-4}$. A Spearman's rank correlation indicates that there is a significant anti-correlation between synchrotron curvature and IC curvature with $p = 4.28 \times 10^{-4}$. However, there are only 9 sources with $|2c^s| > 0.26$, which dominate the correlation analysis, and the scatter of the correlation is large. In this sense, we need more sources with $|2c^s| > 0.26$ to investigate such an anti-correlation.

A strong correlation is found between the two bump peak frequencies, namely $\log \nu_p^{IC} = (0.66 \pm 0.05) \log \nu_p^s + (13.38 \pm 0.81)$ with a correlation coefficient $r = 0.87$ and a chance probability $p < 10^{-4}$, see Fig 4. Because the scatter of the $\log \nu_p^{IC} - \log \nu_p^s$ correlation is about one dex, and $\log \nu_p^{IC}$ is hard to be obtained for some TeV sources, we suggest to use $\log \nu_p^s$ for its estimation.

For the correlation between $\log \nu_p$ and $|2c|$, we have $\log \nu_p^s = -(21.87 \pm 1.04)|2c^s| + (20.01 \pm 0.20)$ with $r = -0.93$ and $p < 10^{-4}$, a Spearman's rank correlation indicates that there is a strongly positive correlation between $\log \nu_p^{IC}$ and $|2c^{IC}|$ with $r = 0.63$ and $p < 10^{-4}$, see Figures 5 and 6.

**Fig. 3** Plot of curvature of inverse-Compton bump against that of synchrotron bump.

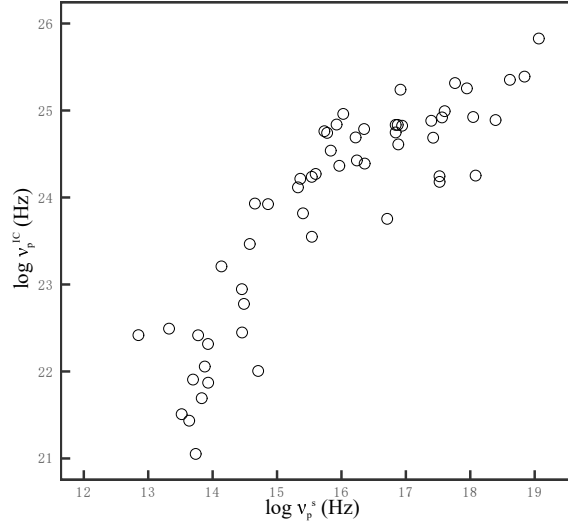


Fig. 4 Plot of peak frequency of inverse-Compton bump against that of synchrotron bump.

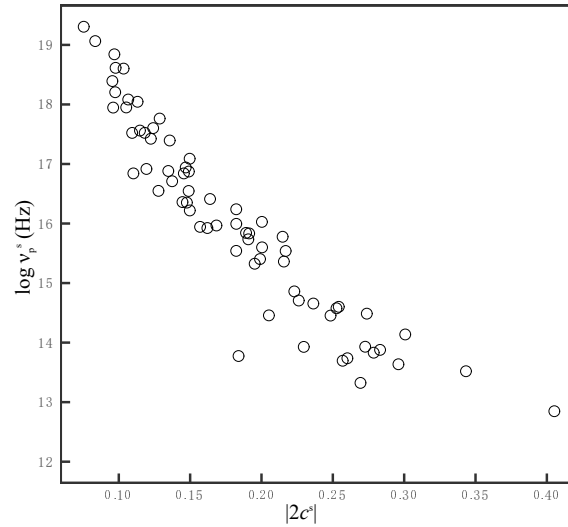


Fig. 5 Plot of peak frequency against curvature for synchrotron bump.

3.2 X/γ-ray Photon Index and Peak Frequency

When the inverse Compton peak frequency ($\log \nu_p^{IC}$) is plotted against the γ -ray spectral index (α_γ), there is a tendency for $\log \nu_p^{IC}$ to decrease with α_γ as shown in Figure 7. Excluding the source 1ES 0229+200, we find a close anti-correlation, $\log \nu_p^{IC} = -(4.59 \pm 0.30)\alpha_\gamma + (32.67 \pm 0.59)$ with $r = -0.90$ and $p < 10^{-4}$.

A clear "L-shape" relation is found between $\log \nu_p^s$ and α_X for TeV blazars, which implies that $\log \nu_p^s$ is highly correlated with α_X , see the upper panel of Figure 8. For the HSP TeV sources ($\log \nu_p^s >$

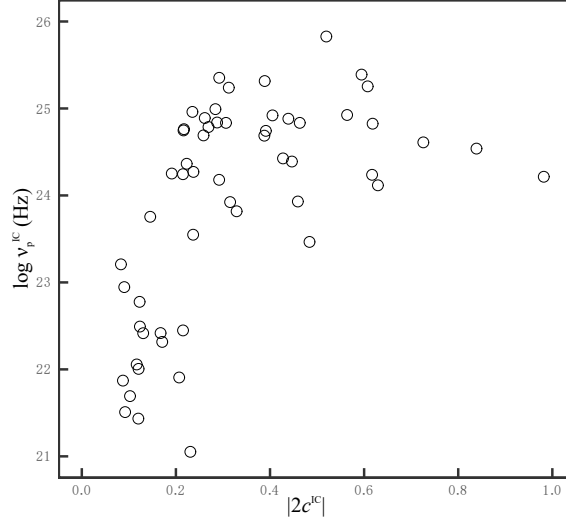


Fig. 6 Plot of peak frequency against curvature for inverse-Compton bump.

15.3 Hz), we have that $\log \nu_p^s = -(3.20 \pm 0.34)\alpha_X + (24.33 \pm 0.79)$ with $r = -0.82$ and $p < 10^{-4}$, and a positive correlation for LSP/ISP TeV sources. Similar result is found for the whole Fermi blazars, see the lower panel of Figure 8. There is a positive correlation between $\log \nu_p^s$ and α_X for ISP/LSP blazars, while there is an anti-correlation between them for HSP blazars. From Figure 8, we found that the changing point of the "L-shape" relation is around $\log \nu_p^s = 15$ Hz, which is very close to boundary between HSP and ISP determined by Abdo et al.(2010) and Fan et al.(2016). Does that mean that we can classify TeV blazars as HSP-TeV and LSP-TeV blazars using $\log \nu_{\text{peak}}^s (\text{Hz}) = 15$?

Another "L-shape" relation is found between α_X and α_γ for TeV blazars. As α_γ increases α_X increases and then decrease, see dot symbols of Figure 9. When we plot the whole Fermi blazars sample in $\alpha_X - \alpha_\gamma$ panel, two separated sub-samples are also obvious, and we can simply use a straight line ($\alpha_X = \alpha_\gamma$) to separate the two sub-samples. TeV blazars mainly occupy the upper-left part of the whole Fermi blazars sample in Figure 9, namely they have softer X-ray and harder γ -ray spectral index than others. The lower-right part sample shows a tendency anti-correlation between α_X and α_γ with $r = -0.28$ and $p < 10^{-4}$, while the upper-left part sample shows a tendency positive correlation between them with $r = 0.29$ and $p < 10^{-4}$, see Figure 9. Our result of the anti-correlation between α_X and α_γ is consistent with those in the work of Wang et al. (1996) and our previous work (Fan et al. 2012). The positive correlation in the present work was not obtained in our previous work because of the sample in our previous work is limited.

3.3 Luminosity-Luminosity Correlation

For luminosity and luminosity correlation, we find that there are strong correlations between peak luminosities and bolometric luminosity, they are:

$\log \nu_p^{IC} L_p^{IC} = (1.28 \pm 0.07) \log \nu_p^s L_p^s - (12.64 \pm 3.21)$ with $r = 0.93$ and $p < 10^{-4}$ for 52 TeV blazars, see Figure 10;

$\log L_{bol} = (1.01 \pm 0.01) \log \nu_p^s L_p^s + (0.82 \pm 0.62)$ with $r = 0.996$ and $p < 10^{-4}$ for 45 TeV BL Lacs, see Figure 11;

$\log L_{bol} = (0.82 \pm 0.03) \log \nu_p^{IC} L_p^{IC} + (9.67 \pm 1.13)$ with $r = 0.98$ and $p < 10^{-4}$ for 52 TeV blazars, see Figure 12.

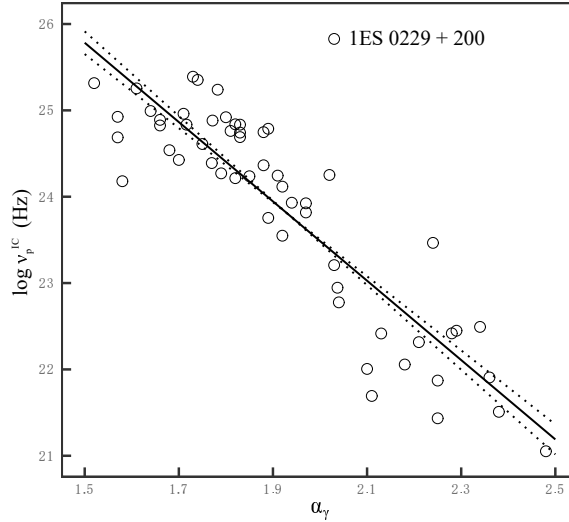


Fig. 7 Plot of inverse-Compton peak frequency against γ -ray photon index. The full line stands for the fitting result ($y = ax + b$) which exclude the source 1ES 0229+200. The dash lines stand for the fitting result with 1σ error, namely $y = (a + \sigma)x + (b - \sigma)$ and $y = (a - \sigma)x + (b + \sigma)$.

Figure 10 shows that $\log \nu_p^{IC} L_p^{IC}$ and $\log \nu_p^s L_p^s$ are closely correlated with each other, and $\log \nu_p^s L_p^s$ is higher than $\log \nu_p^{IC} L_p^{IC}$ for most of TeV BL Lacs, while TeV FSRQs seems to have stronger IC emissions than synchrotron emissions. From Figure 11, we find that FSRQs are the outliers of the $\log L_{bol} - \log \nu_p^s L_p^s$ correlation. So we exclude them when we analyzed the $\log L_{bol} - \log \nu_p^s L_p^s$ correlation.

In this work, the Compton dominance parameter ($CDP = \nu_p^{IC} L_p^{IC} / \nu_p^s L_p^s$) is calculated. Then, the correlation between the bolometric luminosity and CDP is investigated, and a strong correlation, $\log L_{bol} = (1.28 \pm 0.22)CDP + (46.48 \pm 0.10)$ with $r = 0.64$ and $p < 10^{-4}$ is found, see Figure 13. The sources with higher CDPs tend to have higher bolometric luminosity, and FSRQs locate in high $\log L_{bol}$ and high CDPs area. Therefore, the synchrotron emissions are dominant in the bolometric emissions for the most weak power sources, while the IC emissions contribute the main part of power for bright sources.

4 DISCUSSIONS

4.1 Candidates for TeV Blazars

Some researchers proposed TeV blazar candidates based on some selection criteria, "high peak frequency" is a very common one (eg., Massaro et al. 2013; Chang et al. 2017). However, from Table 2, we found that TeV blazars cover a wide range of synchrotron peak frequency, from $\log \nu_p = 12.85$ Hz to $\log \nu_p = 19.31$ Hz. In our sample, 30.4% of blazars are classified as ISP/LSP blazars following our classification criteria (Fan et al. 2016). Thus, if "high peak frequency" are selected as one of the selection criteria of TeV blazar candidates, more than a quarter of TeV sources will be ignored.

From Figure 9, we find that TeV blazars mainly occupy in the left-upper part of the whole Fermi blazars sample. From our previous work (Lin & Fan 2016) and the present work, we found that it is hard to completely separate TeV and non-TeV blazars. In addition, TeV blazars have lower averaged redshift, higher averaged flux, higher peak frequency, flat γ -ray spectrum, stronger γ -ray emissions than

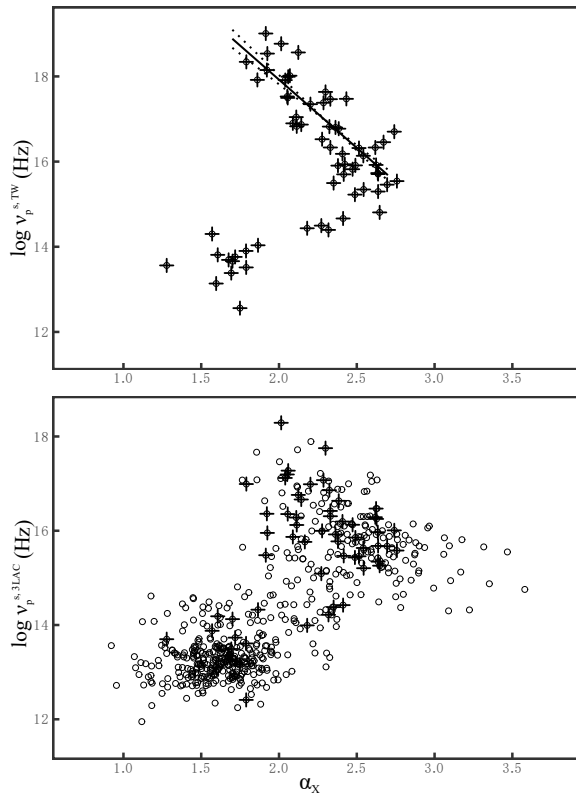


Fig. 8 Plot of synchrotron peak frequency in this work against X-ray photon index for TeV blazars (upper panel), and synchrotron peak frequency in 3LAC (Ackermann et al. 2015) against X-ray photon index for Fermi blazars (lower panel). In the figure, circles stand for the Fermi blazars, and filled circles with cross stand for TeV Fermi blazars. The straight line stands for the fitting result ($y = ax + b$) for HSP TeV blazars. The dash lines stand for the fitting result with 1σ error, namely $y = (a + \sigma)x + (b - \sigma)$ and $y = (a - \sigma)x + (b + \sigma)$.

non-TeV ones. It is possible that all blazars are the emitters of TeV emissions, and TeV blazars are the sources with high TeV flux at certain times.

4.2 Curvature and Peak Frequency

The basic structure of SEDs for blazars can reveal both the radiative and acceleration mechanisms. Tramacere et al. (2007, 2009) analyzed the SEDs of Mrk 421, they found the logarithm of peak frequency to be inversely proportional to the curvature, which indicate the electron energies under stochastic and systematic acceleration. Our recent work (Fan et al. 2016) found a clear anti-correlation between synchrotron peak frequency and curvature for a sample of Fermi blazars (see also Massaro et al. 2004b). In this work, we also find a strong anti-correlation between $\log \nu_p^s$ and $|2c^s|$ for TeV blazars. Thus, our results confirm those results and support the suggestion that the synchrotron SED results from a stochastic and systematic component in the acceleration process. But, the $\log \nu_p - |2c|$ correlations are clearly different for the two bumps, which further indicates that there are different emission mechanisms between them.

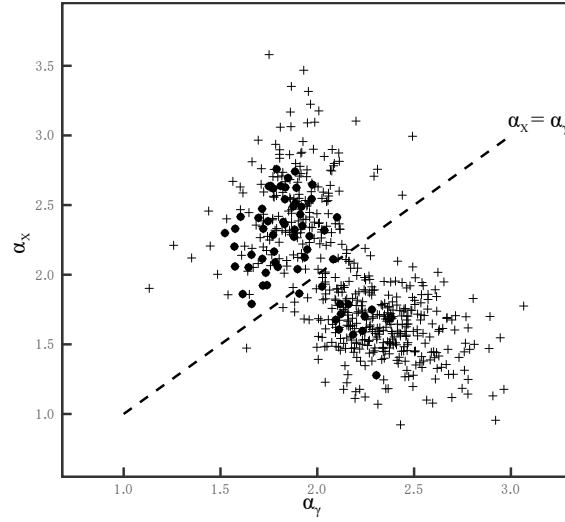


Fig. 9 Plot of X-ray photon index against γ -ray photon index for TeV blazars (filled point symbols), and that for Fermi blazars (plus symbols). The straight dash line stands for $\alpha_X = \alpha_\gamma$.

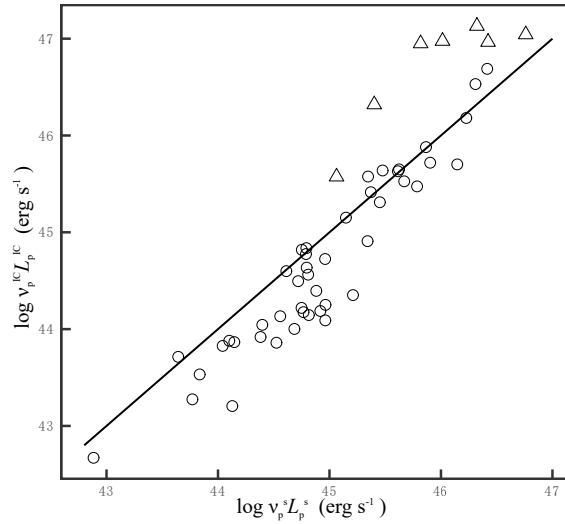


Fig. 10 Plot of IC peak luminosity against synchrotron peak luminosity. The straight line stands for $\log \nu_p^s L_p^s = \log \nu_p^{IC} L_p^{IC}$. The circle symbol stands for TeV BL Lacs, and the triangle symbol stands for TeV FSRQs.

A strong positive correlation is found between the two bump peak frequencies, but the Figure 4 shows that this correlation seems to be a line with a small curved. That means $\log \nu_p^s - \log \nu_p^{IC}$ correlation is a little different between high peak sources and low peak sources. The strong correlation between

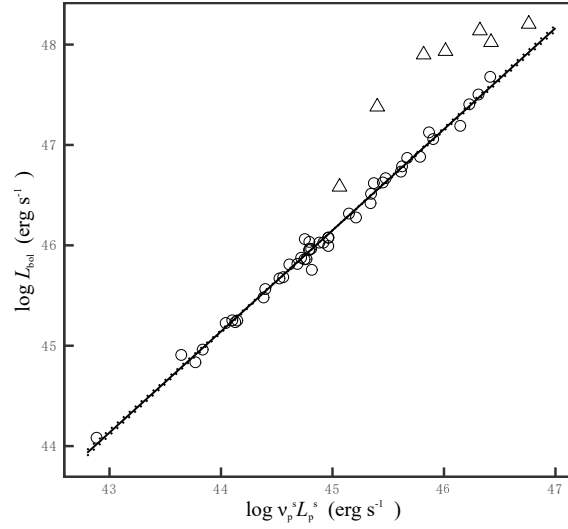


Fig. 11 Plot of bolometric luminosity against synchrotron peak luminosity. The circle symbol stands for TeV BL Lacs, and the triangle symbol stands for TeV FSRQs. The straight line stands for the fitting result ($y = ax + b$) for TeV BL Lacs. The dash lines stand for the fitting result with 1σ error, namely $y = (a + \sigma)x + (b - \sigma)$ and $y = (a - \sigma)x + (b + \sigma)$.

$\log \nu_p^s$ and $\log \nu_p^{IC}$ supports the one-zone leptonic model, indicating that the two bumps are produced by the same electronic population.

4.3 X/ γ -ray Photon Index and Peak Frequency

Abdo et al. (2010b) found that the inverse Compton peak frequency is correlated with the γ -ray spectral index as $\log \nu_p^{IC} = -4.0\alpha_\gamma + 31.6$ for 48 Fermi bright blazars. Since the SEDs fitting results of their work were based on some quasi-simultaneous SEDs, they suggested that the above equation can be used to estimate the $\log \nu_p^{IC}$ of the sources which have no simultaneous SEDs. In this work, we found $\log \nu_p^{IC} = -4.59\alpha_\gamma + 32.67$, which is consistent with the result in Abdo et al. (2010b). Since the detected wavelength of Fermi (1-100GeV) is in an important part of IC bump for blazars, thus the α_γ is an indicator of $\log \nu_p^{IC}$ for blazars.

An "L-shape" relation is found between $\log \nu_p^s$ and α_X in this work for both TeV blazars and Fermi blazars. Abdo et al. (2010b) discussed the behavior between $\log \nu_p^s$ and α_X for 48 Fermi bright blazars, and suggested that the X-ray spectrum will be flat in the LSP sources and the extreme HSP sources. However, there are only a few sources with $\log \nu_p^s > 10^{16}\text{Hz}$ in their sample. Thus, the result of our sample, which covers a wide range of $\log \nu_p^s$, confirms their results. When the peak frequency moves to the lower frequency, the X-ray emissions are composed of the synchrotron tail and the inverse Compton emission resulting in a flat X-ray spectrum index, while the peak frequency is greater than 10^{15}Hz and move to the higher frequency, then the X-ray emission is mainly from the synchrotron emission and results in flat X-ray spectrum again. Therefore, we have an "L-shape" relation between the X-ray spectrum index and the synchrotron peak frequency. We also find that there is no clear difference between TeV and non-TeV sources in $\log \nu_p^s - \alpha_X$ diagram, see lower panel of Figure 8. A significant correlation between $\log \nu_p^s$ and α_X for HSP TeV blazars is also found.

Abdo et al. (2010b) found an anti-correlation between α_γ and α_X , and proposed that such a correlation is excepted at first order in synchrotron-inverse Compton scenarios (see also Wang et al 1996; Comastri et al. 1997; Fan et al. 2012; Ackermann et al. 2015). Fan et al. (2012) found that the $\alpha_\gamma - \alpha_X$

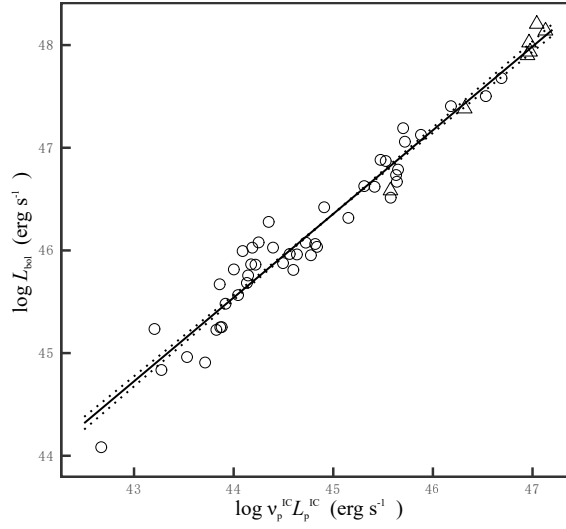


Fig. 12 Plot of bolometric luminosity against IC peak luminosity. The circle symbol stands for TeV BL Lacs, and the triangle symbol stands for TeV FSRQs. The straight line stands for the fitting result ($y = ax + b$). The dash lines stand for the fitting result with 1σ error, namely $y = (a + \sigma)x + (b - \sigma)$ and $y = (a - \sigma)x + (b + \sigma)$.

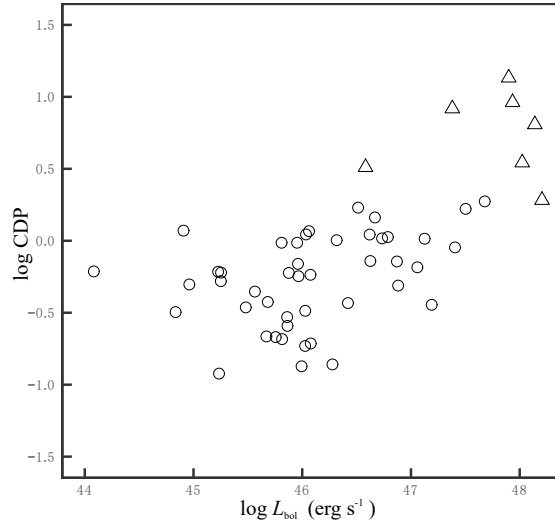


Fig. 13 Plot of Compton dominance parameter against bolometric luminosity. The circle symbol stands for TeV BL Lacs, and the triangle symbol stands for TeV FSRQs.

correlation is not obvious in subclasses of blazars. Figure 9 shows an "L-shape" relation between α_X and α_γ for both TeV blazars and Fermi blazars. For the whole Fermi blazars sample, the $\alpha_X - \alpha_\gamma$ diagram looks like an anti-correlation. However, when we investigated the TeV sub-samples separately, we find a positive correlation between α_X and α_γ at $\alpha_\gamma < 2.0$ range with $r = 0.45$ and $p = 1.91 \times 10^{-3}$.

The anti-correlation is consistent with those in the mentioned works, but the positive correlation was not reported before.

For the two separated sub-groups in Figure 9, we find that the upper-left one corresponds to the sources with $\log \nu_p^s > 15.0$ Hz while the lower-right one corresponds to the sources with $\log \nu_p^s < 15.0$ Hz. Thus, the spectral indexes in X-ray and γ -ray bands are the indicators of the peak frequency of SEDs for blazars. A similar result is also found in $\alpha_{RO} - \alpha_{OX}$ panel, in which HSP sources and LSP sources are located in the different parts of the panel (Abdo et al. 2010b, Fan et al. 2016, and the references therein).

4.4 Bolometric Emissions

In the $\log \nu_p^s L_p^s - \log \nu_p^{IC} L_p^{IC}$ correlation, we find that IC emissions are higher than synchrotron emissions for strong sources whose $\log \nu_p^s L_p^s > 45$ erg/s. From Figures 10 and 11, since $\log \nu_p^{IC} L_p^{IC}$ is larger than $\log \nu_p^s L_p^s$ for TeV FSRQs, the main part of bolometric luminosity should be contributed by IC emissions, which cause the FSRQs to be the outlier in $\log \nu_p^s L_p^s - \log \nu_p^s L_p^s$ correlation. Some researchers also found that FSRQs has higher bolometric luminosity than BL Lacs (eg., Mücke et al. 2003; Giommi et al. 2012; Cha et al. 2014). From Figure 13, it shows that the high power sources ($\log L_{bol} > 46.5$ erg/s) have higher Compton dominance parameter ($\log CDP > 0$).

From above investigation, we can see that the bolometric emissions are highly correlated with both the synchrotron emissions and the IC emissions, and the bolometric luminosity is mainly contributed by synchrotron emissions for BL Lacs, while that is contributed by EC emissions for FSRQs. Therefore, we proposed that the bolometric luminosity can be estimated by the following equation,

$$\log L_{bol} = \begin{cases} 1.01 \log \nu_p^s L_p^s + 0.82 & \text{for BL Lacs} \\ 0.82 \log \nu_p^{IC} L_p^{IC} + 9.67 & \text{for FSRQs} \end{cases}$$

When we compared the estimated bolometric luminosity ($\log L_{bol}^{est}$) using above relations and the bolometric luminosity from the SED fitting, we find that the difference between the two bolometric luminosity ($\log L_{bol}^{est} - \log L_{bol}$) is small, with mean value 0.12, standard deviation 0.07, and max value 0.33 for the sample in this work.

5 CONCLUSIONS

In this work, we collect a sample of 69 TeV blazars from TeVCat, obtain their observations from the SSDC SED Builder, and fit their SEDs by using the second degree polynomial function. The structure parameters of synchrotron bump for 68 blazars and those of IC bump for 56 blazars are obtained, the corresponding statistical values of some parameters, including curvature, peak frequency, peak luminosity, bolometric luminosity, and X/ γ -ray spectral indexes are obtained.

Our main conclusions are as follows:

1. There is a clear positive correlation between the synchrotron peak frequency, $\log \nu_p^s$, and the inverse-Compton peak frequency $\log \nu_p^{IC}$, and that between the synchrotron peak luminosity, $\log \nu_p^s L_p^s$, and the inverse-Compton peak luminosity, $\log \nu_p^{IC} L_p^{IC}$.
2. The correlation between the peak frequency and the curvature of synchrotron bump is clearly different from that of the inverse-Compton bump, which further indicates that there are different emission mechanisms between them.
3. There is a correlation between $\log \nu_p^{IC}$ and γ -ray spectral index, α_γ , for the TeV blazars: $\log \nu_p^{IC} = -(4.59 \pm 0.30)\alpha_\gamma + (32.67 \pm 0.59)$, which is consistent with previous work of Abdo et al.
4. An "L-shape" relation was found between $\log \nu_p^s$ and α_X for both TeV blazars and Fermi blazars. A significant correlation between $\log \nu_p^s$ and X-ray photon index (α_X) is found for the TeV blazars with high synchrotron peak frequency (HSPs): $\log \nu_p^s = -(3.20 \pm 0.34)\alpha_X + (24.33 \pm 0.79)$, while the correlation is positive for LSP TeV sources.

5. In the $\alpha_X - \alpha_\gamma$ diagram, there is also "L-shape", the anti-correlation is consistent with the available results in the literature, we also found a positive correlation between them.

6. Inverse-Compton dominant sources have luminous bolometric luminosities.

ACKNOWLEDGEMENT

The authors thank the referee for the useful comments and suggestions! This work is supported by the National Natural Science Foundation of China (11733001, U1531245), Guangdong Innovation Team (2014KCXTD014), Nature Scientific Foundation of Guangdong Province (2017A030313011), and also supported from Astrophysics Key Subjects of Guangdong Province and Guangzhou City.

References

- Aartsen, M. G., Ackermann, M., Adams, J., et al., 2015, PhRvD, 91b2001
- Abdo, A. A., Ackermann, M., Ajello, M., et al., 2010a, ApJ, 715, 429
- Abdo, A. A., Ackermann, M., Agudo, I., et al., 2010b, ApJ, 716, 30
- Abdo, A. A., Abeysekara, A. U., Allen, B. T., et al., 2014, ApJ, 782, 110
- Abramowski, A., Acero, F., Aharonian, F., et al., 2013, PhRvD, 88j2003A
- Abramowski, A., Aharonian, F., Ait Benkhali, F., et al., 2015, ApJ, 802, 65
- Acciari, V. A., Aliu, E., Beilicke, M., et al., 2008, ApJ, 684L, 73
- Acciari, V. A., Aliu, E., Arlen, T., et al., 2011, ApJ, 738, 169
- Acero, F., Ackermann, M., Ajello, M., et al., 2015, ApJS, 218, 23
- Ackermann, M.; Ajello, M.; Atwood, W. B., et al., 2015, ApJ, 810, 14
- Aharonian, F. A., Akhperjanian, A. G., Barrio, J. A., et al., 2001, A&A, 366, 62
- Aharonian, F., Akhperjanian, A., Beilicke, M., et al., 2003, A&A, 406L, 9
- Aharonian, F., Akhperjanian, A. G., Anton, G., et al., 2009, ApJ, 696L, 150
- Albert, J., Aliu, E., Anderhub, H., et al., 2008, Sci, 320, 1752
- Aller, M. F., Aller, H. D., Hughes, P. A., 1992, ApJ, 399, 16
- Aliu, E., Aune, T., Beilicke, M., et al., 2011, ApJ, 742, 127
- Aliu, E., Archer, A., Aune, T., et al., 2015, ApJ, 799, 7
- Amenomori, M., Ayabe, S., Cui, S. W., et al., 2003, ApJ, 598, 242
- Archambault, S., Arlen, T., Aune, T., et al., 2013, ApJ, 776, 69
- Archambault, S., Aune, T., Behera, B., et al., 2014, ApJ, 785L, 16
- Arlen, T., Aune, T., Beilicke, M., et al., 2013, ApJ, 762, 92
- Bartoli, B., Bernardini, P., Bi, X. J., et al., 2011, ApJ, 734, 110
- Bartoli, B., Bernardini, P., Bi, X. J., et al., 2012, ApJ, 758, 2
- Biteau, J., & Williams, D. A., 2015, ApJ, 812, 60
- Capelo, P. R. & Natarajan, P., 2007, NJPh, 9, 445
- Cha, Y. J., Zhang, H. J., Zhang, X., et al., 2014, Ap&SS, 349, 895
- Chandra, P., Yadav, K. K., Rannot, R. C., et al., 2010, JPhG, 3715201C
- Chandra, P., Rannot, R. C., Yadav, K. K., et al., 2012, JPhG, 39d5201C
- Chang, Y. L., Arsioli, B., Giommi, P., et al., 2017, A&A, 598A, 17
- Comastri, A., Fossati, G., Ghisellini, G., & Molendi, S. 1997, ApJ, 480, 534
- Czerny, B., & Elvis, M., 1987, ApJ, 321, 305
- Daniel, M. K., Badran, H. M., Bond, I. H., et al., 2005, ApJ, 621, 181
- Dermer C. D., Schlickeiser R. et al., 1992, A&A, 256, 27
- Dermer C. D. & Schlickeiser R., 1993, ApJ, 416, 458

- Evans, P. A., Osborne, J. P., Beardmore, A. P., et al., 2014, *ApJS*, 210, 8
- Fan, J.H., 2005, *ChJAA (RAA)*, 5, 213
- Fan, J. H., Huang, Y., He, T. M., et al., 2009, *PASJ*, 61, 639
- Fan, J. H., Yang, J. H., Yuan, Y. H., 2012, *ApJ*, 761, 125
- Fan, J. H., Yang, J. H., Liu, Y., et al., 2015, *IJMPA*, 3045020F
- Fan, J. H., Yang, J. H., Liu, Y., et al., 2016, *ApJS*, 226, 20
- Fossati, G., Maraschi, L., Celotti, A., et al., 1998, *MNRAS*, 299, 433
- Giannios, D., Uzdensky, D. A., Begelman, M. C., 2009, *MNRAS*, 395L, 29
- Giommi, P., Capalbi, M., Focchi, M., et al., 2002, *babs.conf*, 63
- Giommi, P., Polenta, G., Lähteenmäki, A., et al., 2012, *A&A*, 541A, 160
- Godambe, S. V., Rannot, R. C., Chandra, P., et al., 2008, *JPhG*, 35f, 5202
- Hartman, R. C., et al., 2001, *ApJ*, 558, 583
- H.E.S.S. Collaboration, Abramowski, A., Acero, F., et al., 2010, *A&A*, 520A, 83
- H.E.S.S. Collaboration, Abramowski, A., Acero, F., et al., 2013, *MNRAS*, 434, 1889
- Holder, J., 2012, *APh*, 39, 61
- Hovatta, T., Valtaoja, E., Tornikoski, M., Lähteenmäki, A., 2009, *A&A*, 494, 527
- Hovatta, T., Petropoulou, M., Richards, J. L., 2015, *MNRAS*, 448, 3121
- Jones T. W. et al., 1974, *ApJ*, 188, 353
- Kang, S. J., Chen, L., Wu, Q. W., 2014, *ApJS*, 215, 5
- Krawczynski, H., Sambruna, R., Kohnle, A., 2001, *ApJ*, 559, 187
- Kubo, H., Takahashi, T., Madejski, G., et al., 1998, *ApJ*, 504, 693
- Landau, R., Golisch, B. J., Terry J., 1986, *ApJ*, 308, 78
- Lin, C. & Fan, J. H., 2016, *RAA*, 16, 103
- Lin, C., Fan, J. H., Xiao H. B., 2017, *RAA*, 17, 66 (arXiv:170306566L)
- Mannheim, K., Schulte, M., & Rachen, J., 1995, *A&A*, 303, L41
- Marscher A. P., & Gear, W. K., 1985, *ApJ*, 298, 114
- Mastichiadis, A. & Kirk, J. G., 1997, *A&A*, 320, 19
- Massaro, E., Perri, M., Giommi, P., 2004a, *A&A*, 422, 103
- Massaro, E., Perri, M., Giommi, P., & Nesci, R. 2004b, *A&A*, 413, 489
- Massaro, E., Tramacere, A., Perri, M., et al., 2006, *A&A*, 448, 861
- Massaro, F., Paggi, A., Errando, M., 2013, *ApJS*, 207, 16
- Meyer, E. T., Fossati, G., Georganopoulos, M., & Lister, M. L. 2011, *ApJ*, 740, 98
- Mücke, A., Protheroe, R. J., Engel, R., et al., 2003, *APh*, 18, 593
- Nieppola, E., Tornikoski, M., Valtaoja, E., 2006, *A&A*, 445, 441
- Padovani, P. & Giommi, P. 1995, *ApJ*, 444, 567
- Piner, B. G., Pant, N., Edwards, P. G., 2010, *ApJ*, 723, 1150
- Pounds, K. A., Done, C., & Osborne, J. P. 1995, *MNRAS*, 277, L5
- Rees M. J., 1967, *MNRAS*, 137, 429
- Ross, R. R., Fabian, A. C., & Mineshige, S., 1992, *MNRAS*, 58, 189
- Sahu, S., Miranda, L. S., Rajpoot, S., 2016, *EPJC*, 76, 127
- Sambruna, R. M., Maraschi, L., Urry, C. M., 1996, *ApJ*, 463, 444
- Schroedter, M., Badran, H. M., Buckley, J. H., et al., 2005, *ApJ*, 634, 947
- Sharma, M., Nayak, J., Koul, M. K., et al., 2015, *NIMPA*, 770, 42
- Shields, G. A., 1978, *Nature*, 272, 706
- Sikora, M., Begelman, M. C., & Rees, M. J. 1994, *ApJ*, 421, 153

- Sikora, M., et al., 2001, ESASP, 459, 259
- Sokolov, A., & Marscher, A. P., 2005, ApJ, 629, 52
- Tramacere, A., Massaro, F., & Cavaliere, A. 2007, A&A, 466, 521
- Tramacere, A., Giommi, P., Perri, M., Verrecchia, F., & Tosti, G. 2009, A&A, 501, 879
- Urry, C. M., Padovani, P., 1995, PASP, 107, 803
- Wakely, S. P. & Horan, D., 2008, ICRC, 3.1341
- Wang, J. C., Luo, Q., & Xie, G. Z. 1996, ApJ, 457, L65
- Weekes, T. C., 1997, AAS, 191, 3701
- Wu, Q. W., Zou, Y. C., Cao, X. W., 2011, ApJ, 740L, 21
- Wu, Z. Z., Gu, M. F., & Jiang, D. R., 2009, RAA, 9, 168
- Xiong, D. R., Zhang, H. J., Zhang, X., et al., 2013, ApSS, 343, 345
- Xue, R., Luo, D., Du, L. M., et al., 2016, MNRAS, 463, 3038
- Yang, J. H., Fan, J. H., Liu, Y., et al., 2017a, Ap&SS, 362, 219
- Yang, J. H., Fan, J. H., Liu, Y., et al., 2017b, Ap&SS, 362, 22
- Zhang, L., Fan, J. H., Cheng, K. S., 2002, PASJ, 54, 159
- Zhang, J., Liang, E. W., Zhang, S. N., Bai, J. M., 2012, ApJ, 752, 157